VIP Zeolite Films Very Important Paper

International Edition: DOI: 10.1002/anie.201607063
German Edition: DOI: 10.1002/ange.201607063

Nanoscale Control of Homoepitaxial Growth on a Two-Dimensional Zeolite

Meera Shete, Manjesh Kumar, Donghun Kim, Neel Rangnekar, Dandan Xu, Berna Topuz, Kumar Varoon Agrawal, Evguenia Karapetrova, Benjamin Stottrup, Shaeel Al-Thabaiti, Sulaiman Basahel, Katabathini Narasimharao, Jeffrey D. Rimer,* and Michael Tsapatsis**

Abstract: *Nanoscale crystal growth control is crucial for tailoring two-dimensional (2D) zeolites (crystallites with thickness less than two unit cells) and thicker zeolite nanosheets for applications in separation membranes and as hierarchical catalysts. However, methods to control zeolite crystal growth with nanometer precision are still in their infancy. Herein, we report solution-based growth conditions leading to anisotropic epitaxial growth of 2D zeolites with rates as low as few nanometers per day. Contributions from misoriented surface nucleation and rotational intergrowths are eliminated. Growth monitoring at the single-unit-cell level reveals novel nanoscale crystal-growth phenomena associated with the lateral size and surface curvature of 2D zeolites.*

Zeolites, crystalline microporous materials with pores of molecular dimensions, are currently used as catalysts,[1] adsorbents and separation membranes,[2–5] while being considered for new applications.[6,7] Their performance depends mainly on their pore structure, but also on precise control of their crystal shape and size.[8–11] Recent advances in the synthesis of core–shell zeolite catalysts,[12] two-dimensional (2D) and hierarchical zeolites,[13–15] exfoliated zeolite nanosheets,[16,17] and thin zeolite films,[18,19] suggest that nanometer level control of zeolite crystal growth is desirable. However, studies of zeolite crystallization are limited to conventional crystals[20,21] and nanoscale growth events have not been resolved. Herein, growth of a 2D zeolite with nanometer resolution is presented. Conditions leading to slow and controllable growth of 3 nm-thick 2D-MFI nanosheets (for description of MFI structure, see http://www.iza-online.org) with rates of few nanometers per day are identified and provide unprecedented control towards the design of thin films and hierarchical catalysts. Anisotropic growth in the absence of misoriented domains is achieved and allows observation of new crystal growth phenomena associated with the size and local curvature of zeolite nanosheets.

3 nm-thick 2D-MFI nanosheets (thickness of 1.5 unit cell along their *b*-axis) were prepared according to reported exfoliation and purification procedures[16,17] and deposited on Si wafers using a Langmuir–Blodgett trough.[22] They were then calcined in air at 500 °C to remove the occluded structure directing agent (SDA, $C_{22}H_{45}$-$N^+(CH_3)_2$-C_6H_{12}-$N^+(CH_3)_2$-C_6H_{13}·$2\,OH^-$. Nanosheet structural integrity after calcination and their expected *b*-out-of-plane preferred orientation upon deposition on Si wafers were confirmed as reported earlier.[22] It was then attempted to grow these SDA-free Si-supported nanosheets wider, eventually causing them to laterally intergrow, while minimizing increase in thickness and non-oriented growth (owing to rotational and random intergrowths). First, typical MFI growth sols based on tetrapropylammonium hydroxide (TPAOH) were investigated. However, MFI growth with TPAOH as the SDA is prone to a commonly observed orthogonal rotational intergrowth (twinning) causing loss of preferred crystallographic (and pore) orientation. Within 25 min after reaching the growth temperature, the surfaces of MFI nanosheets start to roughen (Figure 1 a), indicating growth by attachment of precursor silica nanoparticles known to be present in these sols.[23,24] The nanosheets progressively thicken (Figure S1 in the Supporting Information), and at 4 h, surface roughness increases and the characteristic morphology of overgrown twins is noticeable (Figure 1 b). Even though oriented films using TPAOH-based sols have been reported in certain cases for conventional MFI crystals,[25–27] it was not possible to find robust conditions transferrable to 2D-MFI nanosheets.

To avoid loss of orientation, the strategy to manipulate crystal-growth rates by altering the SDA[28–30] was adopted. Instead of using TPAOH-based SDA designs, tetraethylammonium hydroxide (TEAOH), known to delay MFI nucleation[31] was selected in an attempt to favor growth by

[*] M. Shete, Dr. D. Kim, N. Rangnekar, D. Xu, Dr. K. V. Agrawal, Prof. M. Tsapatsis
Department of Chemical Engineering and Materials Science
University of Minnesota
421 Washington Avenue SE, Minneapolis, MN 55455 (USA)
E-mail: kimx1408@umn.edu
tsapatsis@umn.edu
M. Kumar, Prof. J. D. Rimer
Department of Chemical and Biomolecular Engineering
University of Houston
4726 Calhoun Road, Houston, TX 77204-4004 (USA)
E-mail: jrimer@central.uh.edu
Prof. B. Topuz
Department of Chemical Engineering, Ankara University
Ankara 06100 (Turkey)
E. Karapetrova
Advanced Photon Source, Argonne National Laboratory
9700 S. Cass Avenue, Lemont, IL 60439 (USA)
Prof. B. Stottrup
Department of Physics, Augsburg College
2211 Riverside Avenue, Minneapolis, MN 55454 (USA)
Prof. S. Al-Thabaiti, Prof. S. Basahel, Dr. K. Narasimharao
Department of Chemistry, Faculty of Science
King Abdulaziz University, Jeddah, 21589 (Saudi Arabia)
Supporting information and the ORCID identification number(s) for the author(s) of this article can be found under http://dx.doi.org/10.1002/anie.201607063.

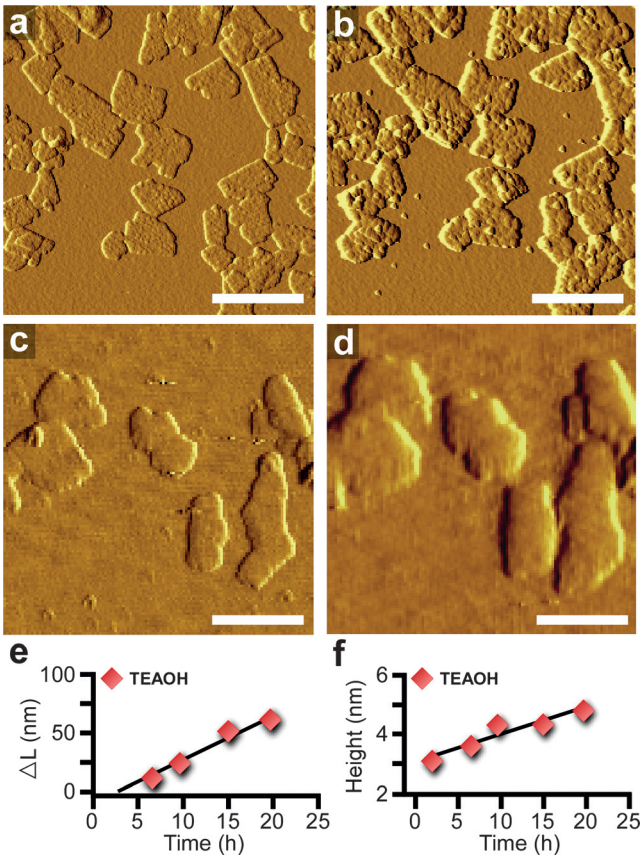

Figure 1. In situ AFM measurements during growth of Si-supported MFI nanosheets. a),b) Amplitude mode images obtained by continuous imaging of MFI nanosheets grown in a TPAOH-based clear sol for a) 0.4 h and b) 4.0 h at 70 °C. c),d) Deflection mode images during continuous imaging of MFI nanosheets grown in a TEAOH-based clear sol of composition 0.198 TEAOH : 0.002 TPAOH : 1 TEOS : 100 H_2O for c) 2.0 h and d) 20 h at 60 °C. e) Change in the lateral dimension of MFI nanosheets in the TEAOH-based clear sol. f) Height evolution of MFI nanosheets grown in the TEAOH-based clear sol. (Scale bars: 500 nm).

homoepitaxy. Indeed, in situ atomic force microscopy (AFM) monitoring of 2D-MFI nanosheet growth with a sol of composition 0.198 TEAOH : 0.002 TPAOH : 1 TEOS : 100 H_2O showed extension of the in-plane and out-of-plane dimensions without surface roughening. Representative images obtained at different times are shown in Figure 1 c (2 h) and Figure 1 d (20 h). Differences in nanosheet morphology evolution in TPAOH- and TEAOH-based sols are striking. In situ AFM indicates surface roughening for TPAOH-based sols, consistent with a contribution to crystal growth by attachment of precursor nanoparticles.[24] However, despite the presence of nanoparticles in optically clear sols of all tetraalkylammonium cations,[23] roughening was not observed for TEAOH-based sol growth. In light of these observations, we hypothesize that TEAOH steers growth predominantly towards a classical pathway via addition of soluble silica species even in the presence of silica nanoparticles that mostly serve as spectators. In-plane growth rate of 4 nm h^{-1} (Figure 1 e) was observed for TEAOH-based sols, while the corresponding out-of-plane growth rate was 0.1 nm h^{-1} (Figure 1 f). This slow growth, likely dominated by molecular species, enables unprecedented control of zeolite crystallization and is worth exploring further. However, the instrumentation used for in situ AFM observations[32] poses limits on the temperature and duration of growth. To access more pronounced nanosheet growth and to completely eliminate the use of TPAOH, we investigated the effect of higher temperatures and longer times in TEAOH-based sols by ex situ AFM.

Similar to in situ AFM studies, a deposit consisting of 2D-MFI nanosheets was formed on Si wafer (Figure 2 a). The same region of 2D-MFI deposit was imaged after growth with a sol of composition 0.2 TEAOH : 1 TEOS: 100 H_2O for 3 days (Figure 2 b). Nanosheet thickening, extension of the in-plane dimensions of nanosheets, and lateral intergrowth were evident. The sample shown in Figure 2 b, was then subjected to a second 3-day growth (Figure 2 c). Tracking the same region after two 3-day growths revealed further merging of nanosheets (Figures S2 and S3). A highly laterally intergrown and thin MFI film was fabricated after four 3-day growths (Figure 2 d). Only ($0\,k\,0$) peaks were detected in the out-of-plane X-ray diffraction (XRD) pattern (Figure 2 e) from the film shown in Figure 2 d, confirming that TEAOH-grown films are *b*-oriented, in contrast to the *a*- and *b*-oriented films using TPAOH-based sols (Figure S4). Consistently, grazing incidence in-plane XRD measurements from uncalcined and calcined coatings and TEAOH-grown films (Figure 2 f) show only the ($h\,0\,l$) peaks. Although in-plane Bragg peaks for the coatings of 2D-MFI nanosheets shift upon calcination (indicating a contraction of the in-plane crystallographic dimensions), peak positions for the TEAOH-grown films exhibit no shift upon calcination due to strong attachment to other nanosheets and the support.[22]

In addition to lateral growth, thickening and appearance of steps on the previously flat nanosheet surfaces are evident (Figures 3 a,b). Representative step heights measured along the marked line-1 in Figure 3 b are plotted in Figure 3 c and show that the steps are predominantly 1 nm in height. Additional measurements of various sheets (Figures S5 and S6) showed that 90 % of the step heights are approximately 1 ± 0.2 nm, which is equal to the height of a pentasil chain, the fundamental building unit of MFI (Figure S7). These observations suggest that under the conditions reported here nanosheet thickening proceeds via 2D nucleation followed by step propagation.

In-plane growth was quantitated by comparing the lateral dimensions of nanosheets before and after growth along their *a*- and *c*-axes (Figures 3 a,b). The direction of maximum in-plane growth was assigned to the *c*-axis on the basis of an earlier report showing that TEAOH leads to faster growth along the *c*-axis.[33] The direction perpendicular to it was assigned as the *a*-axis of nanosheets. Dimensional changes calculated along the *c*- and *a*-axes of nanosheets after growth at different temperature and time are plotted against the corresponding change in thickness in Figure 3 d,e, respectively. The anisotropy ratio—herein, defined as the growth along in-plane directions (*c*- and *a*-axes) versus change in thickness (growth along the out-of-plane *b*-axis)—is plotted against temperature in Figure 3 f. The slow growth along the

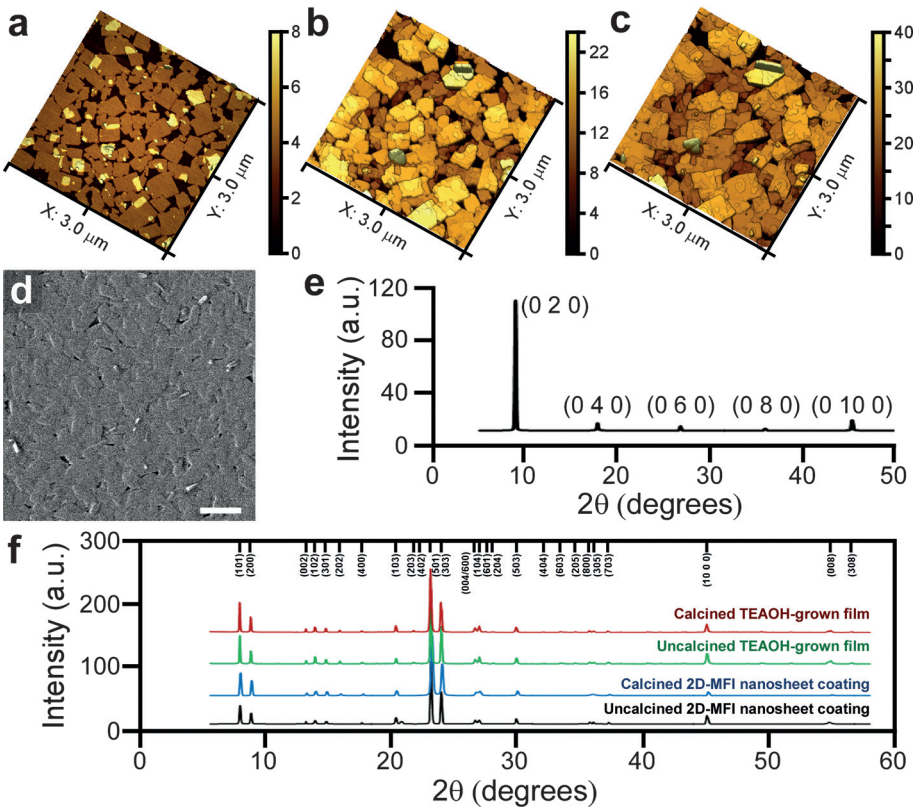

Figure 2. Growth of 2D-MFI nanosheets in TEAOH-based sols. a) AFM 3D height image of 2D-MFI nanosheets supported on Si wafer. b) AFM 3D height image of the same region as in (a) after the first 3-day growth in a TEAOH-based clear sol of molar composition 0.2 TEAOH : 1 TEOS : 100 H_2O at 110 °C. c) AFM 3D height image of the same region as in (a,b) after the second 3-day growth at same conditions (height scale: nm). d) SEM image of a TEAOH-grown MFI film on Si wafer fabricated after four 3-day growths at 110 °C. (Scale bar: 1 micron). e) Out-of-plane XRD pattern from the film in (d); only (0*k*0) peaks are detected confirming that TEAOH-grown films are *b*-oriented. f) Grazing incidence in-plane XRD patterns from calcined and uncalcined 2D-MFI nanosheet coatings and TEAOH-grown films; only (*h*0*l*) peaks are detected confirming the *b*-out-of-plane orientation of nanosheet coatings and TEAOH-grown films.

a-axis in TEAOH-based sols (to be contrasted with similar growth rates along *a*- and *c*-axes in TPAOH-based sols, Figure S8) suppresses the formation of *a*-oriented rotational intergrowths.

The above analysis of growth rates is based on observations from straight edges of nanosheets; however, some of the 2D-MFI nanosheets have fragmented edges resulting from damage during exfoliation and purification (Figure 3 g). These irregularly fragmented edges expose crystal faces other than (100) or (001). It was observed that in-plane growth along the fragmented edges was greater as compared to that along well-defined edges (Figures 3 h,i and Figure S9). Growth rate ratios (growth along the *c*- or *a*-axes of a fragmented edge vs. growth along the same direction for non-fragmented edge) of 2.8 and 1.2 were observed along the nominal *a*- and *c*-axes, respectively. This observation suggests that irregularly fragmented nanosheets can self-heal to regular shapes during lateral intergrowth under the conditions reported herein.

Another important observation is that nanosheets with smaller lateral dimensions thickened less as compared to neighboring larger nanosheets (Figures 4 a,b and Figure S10), which is consistent with thickening rate being determined by the frequency of surface nucleation events (expected to be positively correlated with nanosheet lateral surface area). This finding could have implications in the evolution of film microstructure during nanosheet growth for membrane applications because it suggests that an optimal aspect ratio of nanosheets exists that achieves a balance between the efficient coverage of porous supports (requiring large lateral dimensions) and the reduced propensity to thickening during lateral intergrowth (favored by smaller nanosheets).

Size-correlated suppression in thickening was also evident in cases where a small nanosheet on top (top layer) of a relatively large nanosheet thickened less as compared to the larger underlying nanosheet (bottom layer; see Figure S11). This observation also highlights that layer growth is inhibited when the growth front encounters the misoriented step caused by the top layer. Another case of inhibited nanosheet thickening is also evident when comparing the growth of overlapping bilayer regions with the corresponding growths for the nanosheets involved in the overlap but far removed from the overlap region. In most cases (i.e., 24 out of 26 overlaps investigated), it was seen that the overlapped regions thickened less as compared to the change in thickness determined in the adjacent non-overlapping regions of the nanosheets (Figures 4 c,d and Figure S12). The inhibition of step propagation for steps nucleated on the bottom layer once they encounter the misoriented step caused by the top layer could be understood based on the above discussion of Figure S11. But, what could cause the inhibition of step propagation on the surface of the top layer? Apparently, the surface of the top layer when climbing over the bottom layer adapts a certain curvature causing deviations from its nominal unperturbed crystal structure and this deviation is sufficient to suppress the propagation of steps that have been nucleated in the flat regions. This hypothesis is corroborated by more pronounced cases of surface curvature defects such as wriggles within single nanosheets. Indeed, Figure S13 shows two examples where a wriggle, detectable by AFM, inhibits thickening by propagation of steps nucleated on another region of the same nanosheet.

The slow and controllable growth described here allows for unprecedented nanoscale control of MFI nanosheets and

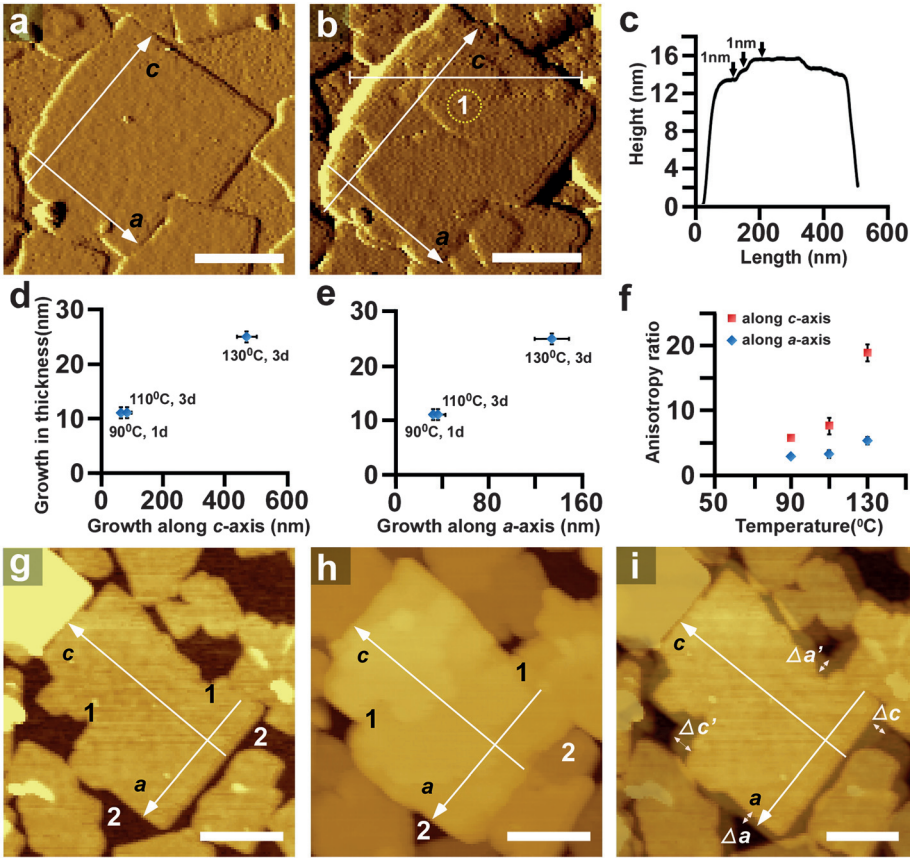

Figure 3. Quantification of nanosheet growth anisotropy in TEAOH-based sols. a),b) AFM amplitude mode images of a MFI nanosheet on Si wafer, before (a) and after (b) growth in a TEAOH-based sol at 110 °C for 3 days. The *a*- and *c*-axes of the nanosheet are indicated. c) Height profile along the marked line-1 in (b) shows that the maximum thickness of the MFI nanosheet after growth is 16 nm with several 1 nm steps evident. d),e) Plots of nanosheet growth in thickness (along *b*-axis) versus growth along *c*-axis (d) and *a*-axis (e) at different temperatures. Data at 90 °C are from a sol composition of 0.198 TEAOH : 0.002 TPAOH : 1 TEOS : 100 H_2O. Data at 110 °C and 130 °C are from 0.2 TEAOH : 1 TEOS : 100 H_2O. f) Plot of anisotropy ratio versus temperature, where anisotropy ratio is the ratio of change of in-plane dimensions (nanosheet growth along *c*- or *a*-axes) over the change in thickness (out-of-plane growth, along *b*-axis). g) AFM height image of a 3 nm thick MFI nanosheet supported on Si wafer showing irregularly fragmented edges (e.g., two regions marked "1" expose crystal faces other than (100) or (001), whereas regions such as the ones marked "2" expose the (100) and (001) crystal planes). h) AFM height image of the same nanosheet shown in (g) after growth in a TEAOH-based sol. i) Superposition of AFM height images shown in (g) and (h) to highlight differences in growth between regions marked "1" and "2". For irregularly fragmented edges, the change in dimensions along *a*- and *c*- are noted as $\Delta a'$ and $\Delta c'$ while the corresponding changes along flat edges are noted Δa and Δc. Typical ratios are 1.2 for ($\Delta c'/\Delta c$) and 2.8 for ($\Delta a'/\Delta a$). (Scale bars: 200 nm).

crystals and is expected to find immediate uses beyond the preparation of thin molecular sieve films and membranes. For example, we found it can also be used to tune the thickness of zeolite domains in hierarchical catalysts. Starting from particles of the material called self-pillared pentasil zeolite (SPP),[15] which are made of single-unit-cell (2 nm thick) MFI nanosheets intergrown orthogonally to each-other to create a house-of-cards arrangement, we were able to controllably thicken the zeolite domains with nm resolution (Figure S14) and preserve the particle morphology. This ability to manipulate the microstructure of thin films and hierarchical catalysts at a scale that approaches single-unit-cell dimensions will offer tremendous potential to improve their properties in a range of commercial applications.

Acknowledgements

This work was mainly supported by the Center for Gas Separations Relevant to Clean Energy Technologies, an Energy Frontier Research Center funded by the US Department of Energy, Office of Science, Basic Energy Sciences under Award DE-SC000105 (all the ex situ AFM experiments reported and the development of the TEAOH-based growth procedure were fully supported by the above award) and by the Deanship of Scientific Research at the King Abdulaziz University D-003/433 (TPAOH-based growth experiments, initial ex situ AFM experiments, certain LB deposition experiments, and XRD characterization). All in situ AFM experiments were performed at University of Houston and J.D.R. acknowledges financial support from the National Science Foundation (Award No. 1151098) and The Welch Foundation (Award No. E-1794). In-plane grazing incidence synchrotron XRD data was collected on beamline 33-BM-C at the Advanced Photon Source, Argonne National Laboratory supported by the U.S. Department of Energy, Office of Science, Office of Basic Energy Sciences, under Contract No. DE-AC02-06CH11357. The LB trough instrumentation purchase and maintenance at the Augsburg College was supported by NSF (DMR 1207544 and CHE 1040126). M.T. acknowledges generous support provided by the Amundson chair fund at the University of Minnesota. Parts of this work were carried out in the Characterization Facility, University of Minnesota and the Minnesota Nano Center (formerly NFC), which receive partial support from the NSF through the MRSEC and NNIN programs, respectively.

Keywords: two-dimensional materials · crystal engineering · crystal growth · nanotechnology · zeolites

How to cite: *Angew. Chem. Int. Ed.* **2017**, *56*, 535–539
Angew. Chem. **2017**, *129*, 550–554

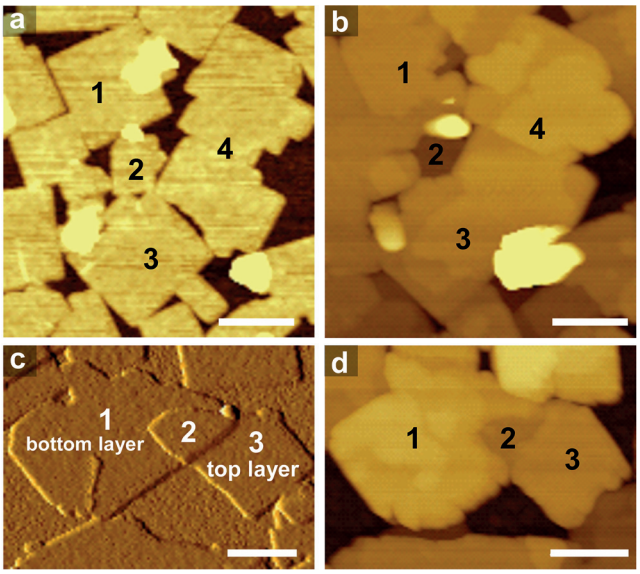

Figure 4. Effect of nanosheet size and curvature on TEAOH-based growth. a) AFM height image of a region with a relatively small nanosheet (marked "2") surrounded by bigger ones ("1", "3" and "4"). b) AFM height image of the same region as in (a) after growth in a TEAOH-based sol of molar composition 0.2 TEAOH : 1 TEOS : 100 H_2O at 110 °C for 3 days. The relatively small nanosheet "2" thickened to 4 nm whereas the larger nanosheets "1, 3, and 4" thickened to 10 nm. c) AFM amplitude mode image of a nanosheet, "3" (top layer-TL), on top of another nanosheet, "1" (bottom layer-BL), giving rise to an overlap region, "2". d) AFM height image of the same region as in (c) after growth in a TEAOH-based sol at 110 °C for 3 days, where the overlap region "2" has thickened to 6 nm as compared to 14 and 10 nm thickening of regions "1" and "3", respectively. (Scale bars: 200 nm.)

[1] A. Corma, *Chem. Rev.* **1997**, *97*, 2373 – 2419.
[2] M. E. Davis, *Nature* **2002**, *417*, 813 – 821.
[3] J. Caro, M. Noack, P. Kölsch, R. Schäfer, *Microporous Mesoporous Mater.* **2000**, *38*, 3 – 24.
[4] M. A. Snyder, M. Tsapatsis, *Angew. Chem. Int. Ed.* **2007**, *46*, 7560 – 7573; *Angew. Chem.* **2007**, *119*, 7704 – 7717.
[5] N. Rangnekar, N. Mittal, B. Elyassi, J. Caro, M. Tsapatsis, *Chem. Soc. Rev.* **2015**, *44*, 7128 – 7154.
[6] T. Bein, *Chem. Mater.* **1996**, *8*, 1636 – 1653.
[7] C. M. Lew, R. Cai, Y. Yan, *Acc. Chem. Res.* **2010**, *43*, 210 – 219.
[8] Z. Lai, G. Bonilla, I. Diaz, J. G. Nery, K. Sujaoti, M. A. Amat, E. Kokkoli, O. Terasaki, R. W. Thompson, M. Tsapatsis, et al., *Science* **2003**, *300*, 456 – 460.
[9] A. Corma, *J. Catal.* **2003**, *216*, 298 – 312.
[10] L. Karwacki, M. H. F. Kox, D. A. M. De Winter, M. R. Drury, J. D. Meeldijk, E. Stavitski, W. Schmidt, M. Mertens, P. Cubillas, N. John, et al., *Nat. Mater.* **2009**, *8*, 959 – 965.
[11] H. Awala, J.-P. Gilson, R. Retoux, P. Boullay, J.-M. Goupil, V. Valtchev, S. Mintova, *Nat. Mater.* **2015**, *14*, 447 – 451.
[12] D. Van Vu, M. Miyamoto, N. Nishiyama, S. Ichikawa, Y. Egashira, K. Ueyama, *Microporous Mesoporous Mater.* **2008**, *115*, 106 – 112.
[13] M. Choi, K. Na, J. Kim, Y. Sakamoto, O. Terasaki, R. Ryoo, *Nature* **2009**, *461*, 246 – 249.
[14] K. Na, C. Jo, J. Kim, K. Cho, J. Jung, Y. Seo, R. J. Messinger, B. F. Chmelka, R. Ryoo, *Science* **2011**, *333*, 328 – 332.
[15] X. Zhang, D. Liu, D. Xu, S. Asahina, K. A. Cychosz, K. V. Agrawal, Y. Al Wahedi, A. Bhan, S. Al Hashimi, O. Terasaki, et al., *Science* **2012**, *336*, 1684 – 1687.
[16] K. Varoon, X. Zhang, B. Elyassi, D. D. Brewer, M. Gettel, S. Kumar, J. A. Lee, S. Maheshwari, A. Mittal, C.-Y. Sung, et al., *Science* **2011**, *334*, 72 – 75.
[17] K. V. Agrawal, B. Topuz, Z. Jiang, K. Nguenkam, B. Elyassi, L. F. Francis, M. Tsapatsis, *AIChE J.* **2013**, *59*, 3458 – 3467.
[18] T. C. T. Pham, T. H. Nguyen, K. B. Yoon, *Angew. Chem. Int. Ed.* **2013**, *52*, 8693 – 8698; *Angew. Chem.* **2013**, *125*, 8855 – 8860.
[19] K. V. Agrawal, B. Topuz, T. C. T. Pham, T. H. Nguyen, N. Sauer, N. Rangnekar, H. Zhang, K. Narasimharao, S. N. Basahel, L. F. Francis, et al., *Adv. Mater.* **2015**, *27*, 3243 – 3249.
[20] J. R. Agger, N. Hanif, S. C. Cundy, A. P. Wade, S. Dennison, P. A. Rawlinson, M. W. Anderson, *J. Am. Chem. Soc.* **2003**, *125*, 830 – 839.
[21] L. I. Meza, M. W. Anderson, J. R. Agger, C. S. Cundy, C. B. Chong, R. J. Plaisted, *J. Am. Chem. Soc.* **2007**, *129*, 15192 – 15201.
[22] N. Rangnekar, M. Shete, K. V. Agrawal, B. Topuz, P. Kumar, Q. Guo, I. Ismail, A. Alyoubi, S. Basahel, K. Narasimharao, et al., *Angew. Chem. Int. Ed.* **2015**, *54*, 6571 – 6575; *Angew. Chem.* **2015**, *127*, 6671 – 6675.
[23] J. M. Fedeyko, J. D. Rimer, R. F. Lobo, D. G. Vlachos, *J. Phys. Chem. B* **2004**, *108*, 12271 – 12275.
[24] T. M. Davis, T. O. Drews, H. Ramanan, C. He, J. Dong, H. Schnablegger, M. A. Katsoulakis, E. Kokkoli, A. V. McCormick, R. L. Penn, et al., *Nat. Mater.* **2006**, *5*, 400 – 408.
[25] Y. Liu, Y. Li, W. Yang, *J. Am. Chem. Soc.* **2010**, *132*, 1768 – 1769.
[26] X. Li, Y. Peng, Z. Wang, Y. Yan, *CrystEngComm* **2011**, *13*, 3657.
[27] Y. Liu, Y. Li, R. Cai, W. Yang, *Chem. Commun.* **2012**, *48*, 6782.
[28] S. L. Burkett, M. E. Davis, *Chem. Mater.* **1995**, *7*, 1453 – 1463.
[29] A. Goretsky, L. Beck, S. Zones, M. Davis, *Microporous Mesoporous Mater.* **1999**, *28*, 387 – 393.
[30] G. Bonilla, I. Diaz, M. Tsapatsis, H. Jeong, Y. Lee, D. G. Vlachos, *Chem. Mater.* **2004**, *16*, 5697 – 5705.
[31] A. Tuel, Y. B. Taarit, *Microporous Mater.* **1993**, *1*, 179 – 189.
[32] A. I. Lupulescu, J. D. Rimer, *Science* **2014**, *344*, 729 – 732.
[33] T. C. T. Pham, H. S. Kim, K. B. Yoon, *Science* **2011**, *334*, 1533 – 1538.

Manuscript received: July 21, 2016
Final Article published: December 9, 2016

